

We are IntechOpen, the world's leading publisher of Open Access books Built by scientists, for scientists

6,900

Open access books available

186,000

International authors and editors

200M

Downloads

Our authors are among the

154

Countries delivered to

TOP 1%

most cited scientists

12.2%

Contributors from top 500 universities



WEB OF SCIENCE™

Selection of our books indexed in the Book Citation Index
in Web of Science™ Core Collection (BKCI)

Interested in publishing with us?
Contact book.department@intechopen.com

Numbers displayed above are based on latest data collected.
For more information visit www.intechopen.com



Characterization of Clay Ceramics Based on the Recycling of Industrial Residues – On the Use of Photothermal Techniques to Determine Ceramic Thermal Properties and Gas Emissions during the Clay Firing Process

Faria Jr. R. T.¹, Souza V. P.¹, Vieira C. M. F.², Toledo R.¹,
Monteiro S. N.², Holanda J. N. F.² and Vargas H.¹
Universidade Estadual do Norte Fluminense Darcy Ribeiro – UENF
¹*Laboratório de Ciências Físicas,*
²*Laboratório de Materiais Avançados,*
Parque Califórnia, Campos dos Goytacazes, RJ
Brasil

1. Introduction

Since Sumerians about 4000 - 3000 BC had created ceramics (Heydorn *et al.*, 1989), the ceramic production has worldwide increased, but the methodology has not suffered substantial evolution in relation to the ancient process. Research work continues to a better understanding of the processes involved and tailoring the desired properties of the final product. The most of ceramists has just worried up with the morphological, physical and structural quality of their products (Okada *et al.*, 1986; Dubois *et al.*, 1995; Nastro *et al.*, 2006). However, one of the main ceramics features was not yet well concerned by the community, that is, its thermal behaviour. Urban buildings of equatorial and tropical countries are often subjected to constant solar radiation. Thus, thermal properties play a significant role in the quality of end-products. A better indoor ambient of the houses should be ever pursued. While technological properties of those materials are frequently found in the literature, information about the thermophysical characteristics of red ceramics is very scarce (Alexandre *et al.*, 1999).

In the early eighties, a new physical device to generate and detect thermal waves was proposed (Vargas and Miranda, 1988). It has been widely used in last few years as a tool to measure the thermal properties of a large range of materials (Marín *et al.*, 2002; Faria *et al.*, 2005). The photoacoustic (PA) technique via OPC (an open photoacoustic cell) is used to evaluate the thermal diffusivity, an important parameter that determines the light-to-heat conversion efficiency, and furthermore, it allows us to study how heat diffuses through the sample (Perondi and Miranda, 1987). The thermal diffusivity is an intrinsic property of matter. Moreover, it is dependent upon the effects of composition and microstructural variables, as well as processing conditions. Thermal properties are very sensitive to

amorphous–crystalline phase transitions of clays heated above 900 °C, typical temperatures applied in the manufacturing process of ceramic materials.

Clay deposit areas have a high economic potential, and soil mineralogical composition, plasticity and porosity are fundamental properties for industrial applications. The resulting ceramic products present a network of capillary pores that vary according to the firing cycle. Important ceramic properties such as hardness, water absorption, gas permeability, shrinkage, density, thermal properties, gas emission as well as the vitrification temperature range are intrinsically correlated to the porous system (Rice and Dekker, 1998).

In addition, the whole world presently draws increasing attention to the environment, requiring the adjustment of industrial activities according to laws and norms that rule the sector. Thus, increasing environmental problems related to climate changes and pollution are going attention and raising special concern regarding to the dispersal of industrial wastes. As a consequence, the society is demanding not only actions towards waste reduction but also measures for redirecting or post-using wastes mainly those of industrial origin. Most of the residues generating in the production process is normally handled by land disposal in certain areas, thus recycling of these residues may produce the value-added products and prevent environmental deterioration. As solid wastes are becoming a matter of increase world concern due to their amount as well as difficulty and cost of final disposal, ceramic products can well supply as matrices for industrial residues incorporation such as giving an option for the solid waste disposal with a possible increase in the properties of the clay ceramic products. The incorporation of wastes from several industrial activities is a technological alternative to reduce the environmental impact due to their indiscriminate disposal. One such a measure is the waste incorporation into intensive-produced clay ceramics like bricks and tiles (Parsons *et al.*, 1997). This incorporation is now a common practice and benefits both, the industry that generates the waste and the ceramic industry that saves on the clay, which is its basic raw material. In some cases the incorporation also improves the properties of the ceramic product (Oliveira and Holanda, 2004).

Research works on the structural and physical changes that wastes, mainly industrially produced, cause to the final ceramic product has been rapidly expanding in these last two decades. See, for instance references in (Vieira and Monteiro, 2009). In spite of these examples of a continuous effort to incorporate wastes into clay ceramic motivated by technical and economical advantages, environmental issues are still a matter of concern. The firing stage during the clay ceramic process can promote the elimination of potentially toxic constituents present in the solid residues through their volatilization. However, the gas emission due to the clay firing process and its related atmospheric pollution may be enhanced as a consequence of an incorporated waste (Souza *et al.*, 2008). It is known that the firing of clay ceramics in conventional furnaces using fuels such as wood, charcoal, heavy oil and natural gas generates appreciable amounts of gaseous components, mainly carbon dioxide (CO₂), carbon monoxide (CO) and methane (CH₄). Additionally to the atmospheric pollution, these gas sets could be harmful to the human health and can corrode equipments (Morgan, 1993).

Works on the effect of gas emission caused by the firing of clay ceramics incorporated with industrial wastes are practically inexistent. Therefore one of the mean objectives of this chapter was to investigate the gas emission resulting from the firing of clay ceramics incorporated with different industrial residues. Here, slag type of waste from steel refining operation and sanitary ware mass wastes were the selected residues.

In order to show methodologies to characterize ceramics here depicted, the samples under study were clay from Rio de Janeiro state and from São Paulo state. Firstly, the raw materials without residues is presented and throughout characterized. In a second stage, the aggregation of the residues is pointed out. Characterizations are performed and compared with the clays without residues.

2. Ceramic samples

Clayey soils from two sites of the Southeast Brazilian region were studied for the production of red ceramics. The samples preparation was pointed out in the following.

2.1 Kaolinite clay from Rio de Janeiro state (CG clay)

The raw material was collected from a quaternary sedimentary basin situated in Campos dos Goytacazes, from a layer localized between 0.30 m and 1.80 m below the surface, where large clay deposits are quarried as raw material for red bricks and tiles. About 20 kg of material collected in situ were dried, grounded, and passed through a sequence of sieves yielding a homogeneous powder with particle size smaller than 75 μm , corresponding to 95 % of the original mass.

For technological measurements, a quantity of the powder was mixed with water and then extruded at 36 MPa into a rectangular prismatic mould with a 20x10 mm cross-section, cut into bars 100 mm long which were left drying in air for two weeks at room temperature. Before the firing process, the samples were subjected to an additional drying cycle in an oven at $(110 \pm 5 \text{ }^\circ\text{C})$ for 24 hours. Then, the sample weight and dimensions were measured just before starting the firing process. X-ray diffraction measurements were done on the same samples used for technological measurements.

To simulate the continuous sintering process of the ceramic material up to 1200 $^\circ\text{C}$, and to accompany the changes that occur, 13 thermal treatment steps were chosen, each step being denoted T_F henceforth. For firing temperatures up to 600 $^\circ\text{C}$ the heating rate was set to 2 $^\circ\text{C}/\text{min}$. Once the desired T_F was reached, the sample was left at constant temperature for 3 hours, and then cooled down to room temperature at a rate of 1.5 $^\circ\text{C}/\text{min}$. For T_F above 600 $^\circ\text{C}$, the heating cycle was such that the sample was heated at a rate of 2 $^\circ\text{C}/\text{min}$ up to 600 $^\circ\text{C}$, left at this temperature for one hour, and then heated at a rate of 10 $^\circ\text{C}/\text{min}$ up to the selected firing temperature, where it was left for 3 hours before cooling down to room temperature at a rate of 1.5 $^\circ\text{C}/\text{min}$.

To perform the thermal characterization the raw material was passed through a sieve with nominal aperture of 75 μm (mesh 200 ASTM). In order to prepare the samples for analysis, a press (SHIMADZU) was used. 90 mg of each sample was weighed and submitted to a 9 tonne pressure for 10 minutes, using disc samples with 10 mm diameter and a thickness between 200 μm and 500 μm . After that, the samples were fired in a furnace (MAITEC 12 kW/32 A) at six different temperature steps, ranging from 900 to 1100 $^\circ\text{C}$.

Finally, to analyse the gas emissions from the CG clay and its residue, rectangular 114.5 x 25.4 x 10 mm samples with 8 % of humidity were 20 MPa moldpress by mixing the clay with different amounts of 5 and 10 wt% of steel slage. Samples of pure clay were also considered for comparison. All samples were initially dried at 110 $^\circ\text{C}$ in a laboratory stove and then fired in a continuous way, from room temperature to a maximum of 1100 $^\circ\text{C}$, inside a tubular model FT-1200 BI, MAITEC electrical furnace. The firing was conducted at a heating rate of 2 $^\circ\text{C}/\text{min}$ from RT to 500 $^\circ\text{C}$ and 4 $^\circ\text{C}/\text{min}$ between 500 and 1100 $^\circ\text{C}$.

2.2 Illitic clay from São Paulo state (J clay)

The raw material was collected from a neocenoic sedimentary soil placed in Jundiaí city, 60 km far from São Paulo city in São Paulo state. The preparation process was similar to the sample of Campos dos Goytacazes for both applications. However, the J clays do not have such plasticity as CG clays. According to their chemical properties (sub-section 3.1), they can be considered fluxes clays mainly by the alkaline elements (K_2O , CaO and MgO), which are responsible for the ceramic sintering. The value of K_2O comes from the mineral illite, while $CaO + MgO$ are linked with calcite and dolomite minerals. Al_2O_3 is related mainly to the kaolinite mineral.

3. Characterization by X-Ray

The chemical composition and crystalline phases of the raw material with and without residues and only of the residues were presented. The microstructure of the samples as in function of the firing temperature was represented by X-ray diffractions.

3.1 Energy dispersive X-Ray fluorescence

Using X-ray fluorescence spectrometry methods described in previous work Mota *et al.*, 2008), the percentual contribution of the main oxides present in our material was determined.

The chemical characterizations were obtained by energy dispersive X-ray spectroscopy (EDS), using a SHIMADZU equipment. The resulting values of this quantitative analysis from CG clay and its steel slag residue and from J clay and its sanitary ware mass residue are shown in Table 1 and Table 2, respectively.

Observing Table 1 and Table 2 we can classify CG clay as kaolinite-based clay (higher Al_2O_3) and J clay as illitic-based clay (higher fluxes oxides), as explained in the previous section. In addition to SiO_2 and Al_2O_3 , there are considerable amounts of Fe_2O_3 , K_2O and TiO_2 , which is favourable for red ceramics production. Iron oxide accounts for the bodies' red pigmentation after firing.

Oxides in wt%	CG Clay	Steel slag residue
SiO_2	46.42	10.29
Al_2O_3	27.90	21.5
MnO	0.11	5.40
MgO	0.71	10.33
CaO	0.22	45.10
Na_2O	0.36	-
K_2O	1.67	-
TiO_2	1.32	0.34
Fe_2O_3	9.10	*
P_2O_5	-	1.85
SO_3	-	0.54
SrO		0.18
LoI	11.96	12.96
* Total Fe from the residue (%) - 23.62		

Table 1. Chemical composition of the CG clay and steel slag (% in weight). The slag predominantly is formed by composites of Ca, Al, Fe, Mg and Si

Oxides in wt%	J Clay	Sanitary ware mass residue
SiO ₂	59.61	64.8
Al ₂ O ₃	21.19	21.5
MnO	0.05	0.06
MgO	1.07	0.78
CaO	0.33	0.32
Na ₂ O	0.12	0.51
K ₂ O	2.33	2.53
TiO ₂	0.94	0.89
Cr ₂ O ₃	-	0.05
P ₂ O ₅	0.13	0.13
SO ₃	-	0.06
Fe ₂ O ₃	5.45	5.96
ZnO	-	0.03
ZrO ₂	-	0.13
LoI	9.28	2.25

Table 2. Chemical composition of the J clay and the sanitary ware mass residue (wt.%). The residue is a silt-clay with very low plasticity which should enhance the structural quality of the ceramic

3.2 X-Ray diffraction

The X-ray diffraction experiments were performed at room temperature Using the Co-K α or Cu-K α radiation of a Seifert URD65 diffractometer, equipped with a diffracted beam graphite monochromator. The CG clay diffractograms were obtained from 3 to 50° using the Co-K α , while the slag steel residue from 3 to 70°. The J clay diffractograms were obtained from 3 to 75° with step sizes of 0.03° and accumulation time of 3 s. From the diffractograms the sample crystallinities were determined as the ratio between the integrated intensity of the sharp diffraction peaks to the total area of the diffraction pattern, which includes the non-coherent intensity. The CG clay sample was thoroughly analysed as in function of the firing temperature, whereas the J clay was just analysed the 110 °C sample.

Fig. 1 shows the XRD patterns as a function of the firing temperature TF. A quantitative phase analysis was performed for the natural powdered soils of Campos dos Goytacazes using the Rietveld refinement method (Manhães *et al.*, 2002). The Rietveld analysis was performed considering the angular range 10° < 2 θ < 70°, thus not taking into account the illite phase due to its peak shape. Kaolinite is the main crystalline phase with 86% mass fraction, followed by quartz (5%), anatase (5%) and gibbsite (4%).

The diffractograms of the samples treated up to 400 °C show a similar mineral composition with kaolinite as the major phase. Between 400 and 500 °C the kaolinite dehydroxylation occurs, with the transformation to a non-crystalline phase, metakaolin: Al₂Si₂O₅(OH)₄ → Al₂Si₂O₇+2H₂O↑. The other crystalline phases (illite and quartz) remain unchanged up to 900 °C. For this temperature range no more organic material is present in the amorphous component. . The main crystalline phases present in our non-treated samples were kaolinite (Al₂Si₂O₅(OH)₄), quartz (SiO₂), anatase (TiO₂), gibbsite (Al(OH)₃), goethite (FeO(OH)) and illite ((K,H₃O)Al₂Si₃AlO₁₀(OH₂)), while the sinterized samples showed the presence of

mullite ($\text{Al}_6\text{Si}_2\text{O}_{13}$), cristobalite (SiO_2) and hematite (Fe_2O_3). Quantitative phase analysis using the Rietveld refinement method showed that kaolinite is the main crystalline phase responding for approximately 86 wt. %.

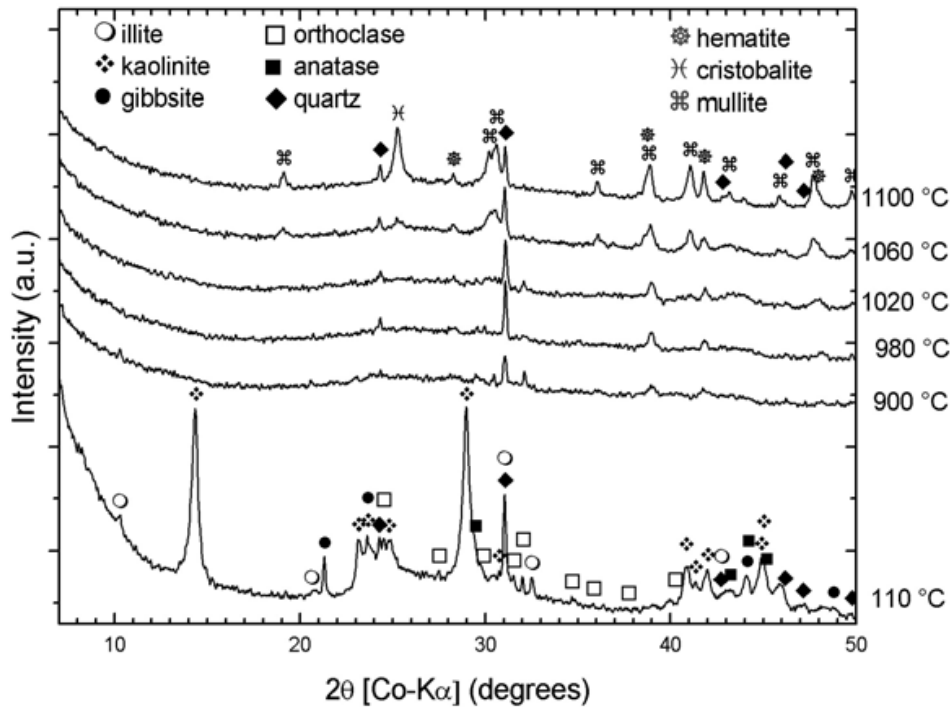


Fig. 1. X-Ray diffractograms of CG clay as in function of firing temperature

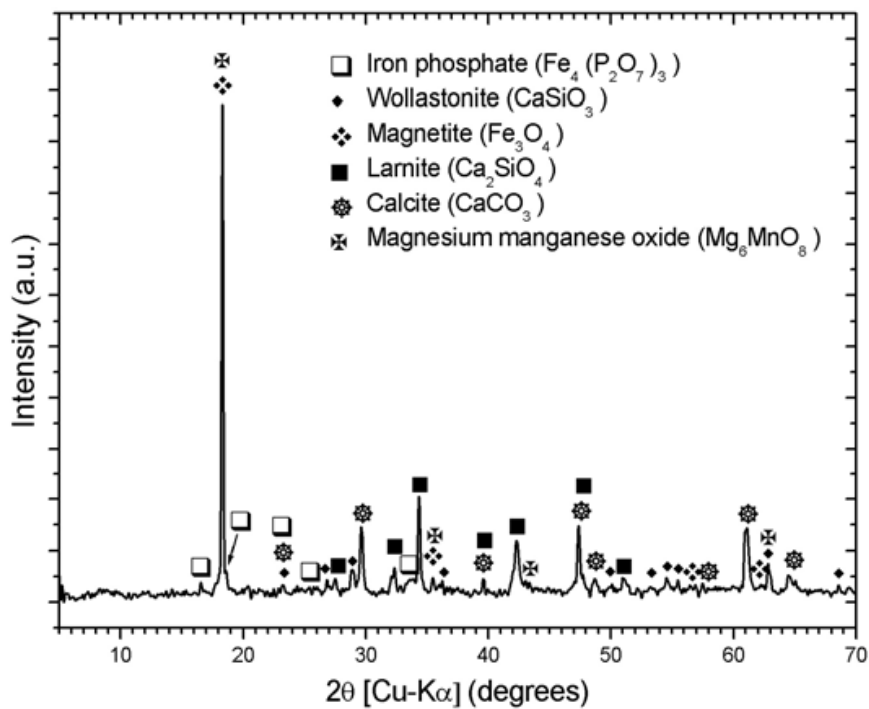


Fig. 2. Steel slag residue as processed diffractogram

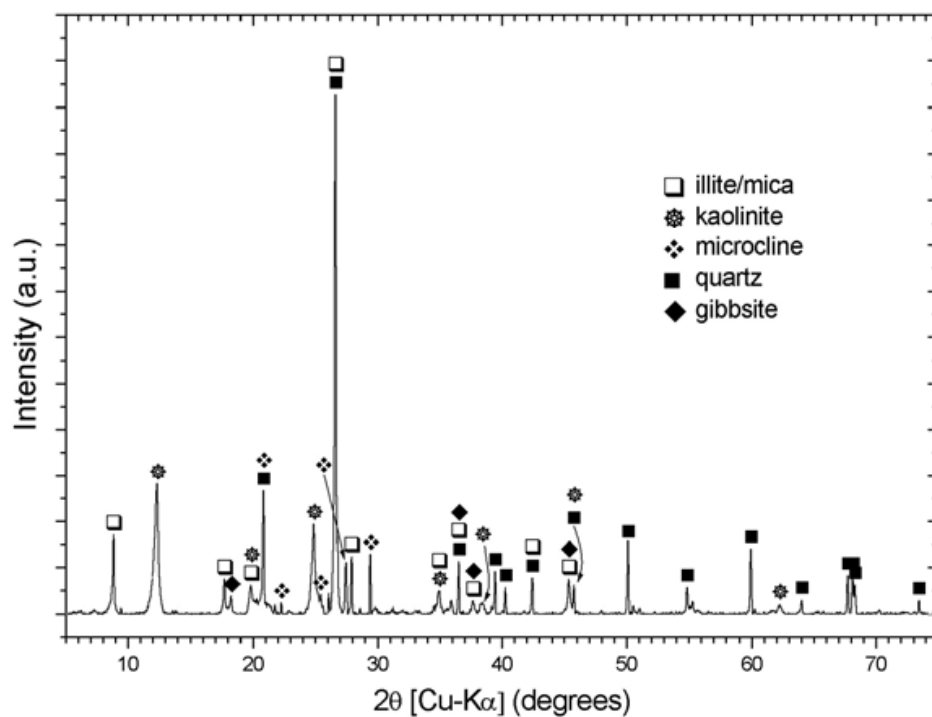


Fig. 3. X-ray diffractogram of J clay at room temperature

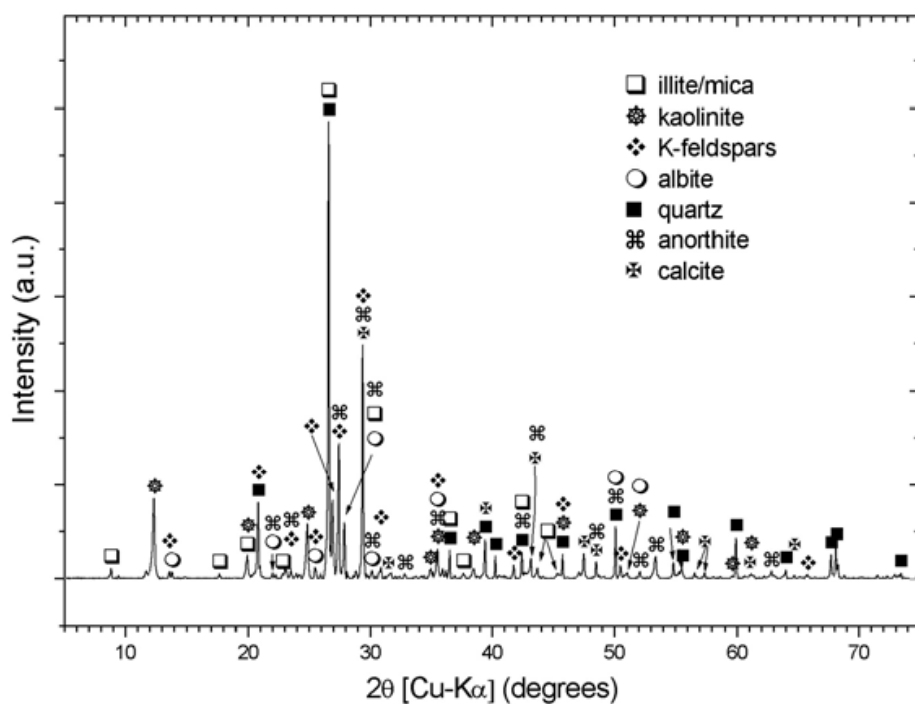


Fig. 4. X-ray diffractogram of the sanitary ware mass residue

Fig. 2 shows the X-rays diffraction pattern of the steel residues. In the respective figure the predominantly formed crystalline phases of Ca and Fe had been identified to associate diffraction peaks. The rich phases in calcium (Ca) are silicates and the calcite. On the other

hand, iron (Fe) is present in the form of magnetite and iron phosphate. Diffraction peaks of the magnesium manganese oxide were identified. In accordance to Fig. 2, Ca is present in the wollastonite (CaSiO_3) and larnite (Ca_2SiO_4) form and also as carbonate (calcite - CaCO_3). Mg and Mn are presented as magnesium manganese oxide (Mg_6MnO_8), while Fe is given in form of magnetite (Fe_3O_4).

Fig. 3 shows the XRD patterns of the J clay raw material. This diffractogram indicates the presence of a micaceous mineral, quartz, microcline, gibbsite and kaolinite.

Fig. 4 points out the sanitary ware mass diffractogram, which shows the presence of micaceous material, albite, anorthite, k-feldspars, clay minerals, quartz, and calcite. We observed a variety of flux materials. Feldspars and microcline are sources of alkaline flux materials, such as K_2O and Na_2O , which make possible the formation of a liquid phase above $700\text{ }^\circ\text{C}$ (Reed, 1976). The fluxing capacity of this residue, which is associated with lower porosity after firing, is also confirmed by the presence of K_2O and Na_2O containing minerals. Then, the sanitary ware mass is the source of K_2O and Na_2O , which act as fluxes to improve the sintering process.

4. Technological essays

4.1 Density and porosity measurements

The samples dimension and mass were measured before and after each firing cycle so that the volumetric shrinkage and bulk densities could be straightforwardly determined.

Between 500 and $1200\text{ }^\circ\text{C}$, the porosity measurement consisted in measuring first the mass of the dry sample after firing at temperature T_F , denoted henceforth as m_{TF} , then two water-saturated sample masses: one, denoted as m_i , inside water after 2 h boiling, the other, denoted as m_o , outside taking care to remove the excess water from the sample surfaces. The sample open porosity was obtained as the ratio $(m_o - m_{TF}) / (m_o - m_i)$.

For samples that undergone heat treatments at 110 , 300 and $400\text{ }^\circ\text{C}$, we have adopted the conventional pycnometer method, the reason for this being that these samples usually exhibit larger porosity and lower particle cohesion than those treated at higher temperatures. In this way, we have avoided eventual sample disintegration due to prolonged water immersion.

4.2 Mechanical testing

The flexural rupture tension of our samples was determined by a universal testing machine using the three-point loading test with a crosshead speed of 0.1 mm/min , designed following the ABNT standard procedure¹⁷, method equivalent to ASTM C67. The bending strength was calculated from the breaking load using the relation $BS = 3PL/2bd^2$, where P is maximum load, L is the distance between the supports of the beam, b is the brick average width and d is the brick average depth.

Figure 5 indicates that after $1000\text{ }^\circ\text{C}$ the open porosity decreases abruptly from 39.6% to 5.6% , while the volumetric shrinkage and the bending strength both exhibit a large increase from 16.8% to 40.0% and from 9.0 MPa to 25.2 MPa , respectively. These results together with the X-ray diffraction data indicate that these changes are associated with recrystallization and sintering processes setting in between 1000 and $1200\text{ }^\circ\text{C}$ with the formation of mullite, cristobalite, and hematite phases, with great improvement of the ceramic properties. To further strength this aspect we present in Fig. 6 the correlations of the sample density, bending strength and volumetric shrinkage with the sample crystallinity, in

the temperature range above 1000 °C. The solid lines in this figure correspond to the data linear regression. These results indicate that, indeed, these physical properties are all well correlated with the crystallinity changes taking place in our sample in this temperature interval.

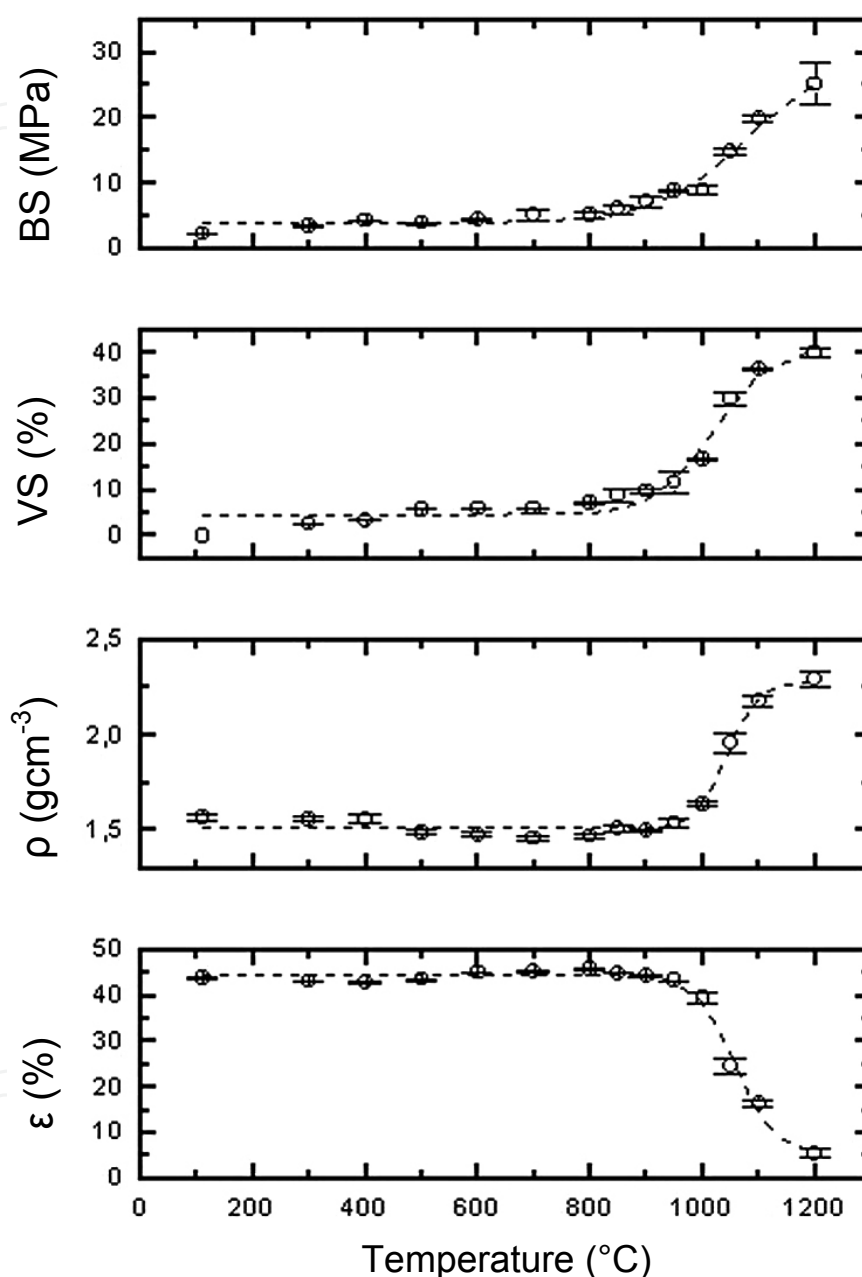


Fig. 5. The dashed lines in the bending strength, volumetric shrinkage, density and porosity plots correspond to the data fitting using a logistic function (Eq. 1)

In Fig. 5 we present the evolution of the technological properties (bending strength (BS), volumetric shrinkage (VS), bulk density (ρ) and open porosity (ϵ)) as a function of the firing temperature. In order to single out the temperature point at which the phase transitions taking place in our sample affect most the corresponding physical properties we have performed a fitting of our data to a logistic curve of the following form,

$$f(T) = A + B \frac{\exp((T - T_0) / \Delta T)}{1 + \exp((T - T_0) / \Delta T)}, \quad (1)$$

where A , B , T_0 and ΔT are all adjustable parameters. The dashed lines Fig. 5 correspond to this logistic data fitting. In Eq. 1, T_0 indicates the point at which the transition occurs whereas ΔT gives us an idea of how wide this transition is. The resulting values obtained from this data fitting procedure for the parameters T_0 and ΔT are summarized in Table 3.

Data	T_0 (°C)	ΔT (°C)
Open Porosity (ϵ)	1057.03	35.62
Bulk Density (ρ)	1042.57	28.00
Volumetric Shrinkage (VS)	1021.61	52.68
Bending Strength (BS)	1079.97	80.39

Table 3. Values of the data fitting parameters characterizing the temperature and its excursion where the main changes of the physical properties of our samples occur

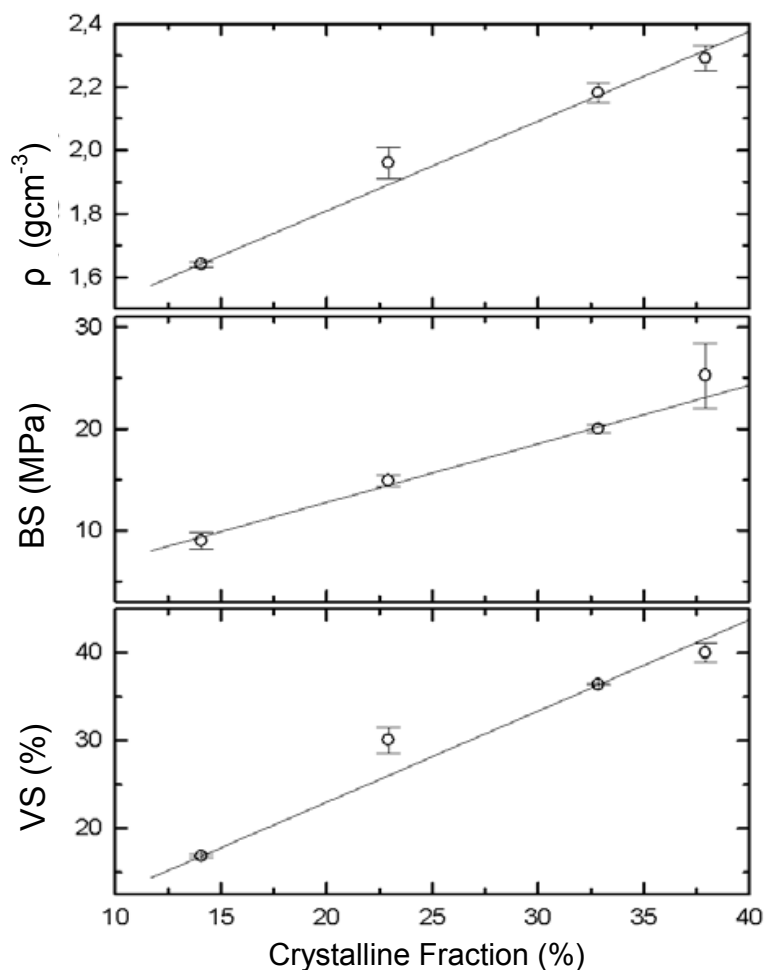


Fig. 6. Correlations of the sample density, bending strength and volumetric shrinkage with the sample crystallinity, in the temperature range above 1000 °C. The solid lines correspond to the data linear regression

The data shown in Fig. 6 also suggest some other interesting correlations among the different measured physical properties. For instance, the changes in bending strength and the volumetric shrinkage, as well as those of the porosity and density, seem to be well correlated.

We present in Figs. 7 and 8 the correlations between these physical properties. The straight lines in these figures correspond to the data linear regression. It follows from Fig. 6 that the bending strength and the volumetric shrinkage are well correlated up to 1050 °C, at which point a sharp discontinuity in the correlation takes place.

As to the correlation between the sample porosity and density, shown in Fig. 5, the same behaviour is observed, that is, a good correlation among these properties up to 1050 °C followed by a sharp discontinuity at this temperature. These critical transitions taking place around 1050 °C, are in good agreement with the values found from the logistic data fitting for T_0 , as shown in Table 3, as well as with the argument presented above indicating that a sintering process is set in around this temperature.

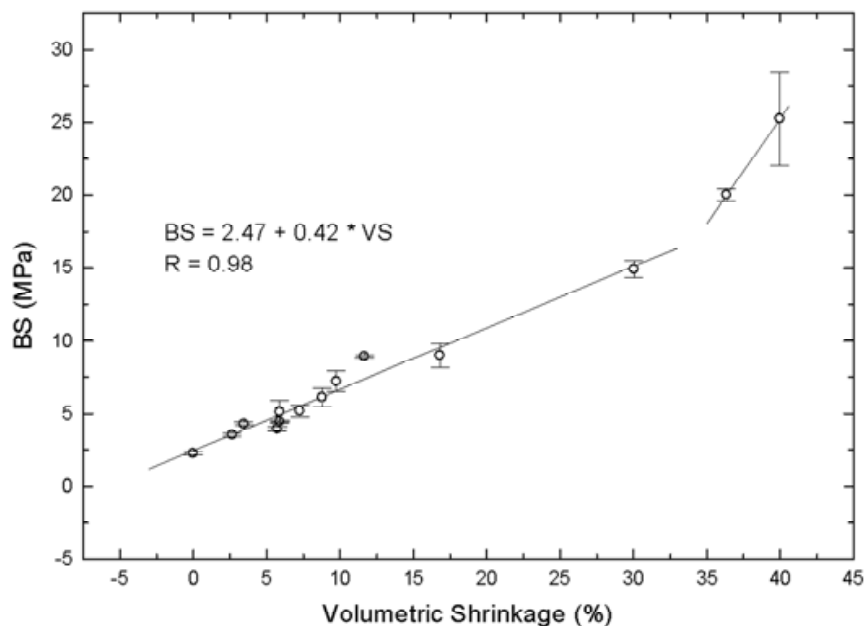


Fig. 7. Correlation between the bending strength and the volumetric shrinkage. The straight lines correspond to the data linear regression

The phase transformations from X-ray diffraction data are well known. Up to 400 °C the dominant phase transformations are due to intense dehydroxylation processes of components, such as gibbsite and goethite, with kaolinite remaining as the major mineral phase. Between 400 and 500 °C, we observed a reduction in crystalline fraction, due the transformation of kaolinite to a noncrystalline phase, metakaolinite ($\text{Al}_2\text{Si}_2\text{O}_5(\text{OH})_4 \rightarrow \text{Al}_2\text{Si}_2\text{O}_7 + 2\text{H}_2\text{O}$) took place, while the other crystalline phases (quartz, anatase and illite) remained unchanged up to 900 °C. Heat treatments above 1000 °C cause new structural changes with the formation of mullite, cristobalite, and hematite phases, among others.

Considering the technological measurements of the J clay and the sanitary ware mass residue, Table 4 presents the technological properties of volumetric shrinkage, bending

strength and water absorption for the product fired at 980 °C, considered the best temperature for commercial purposes.

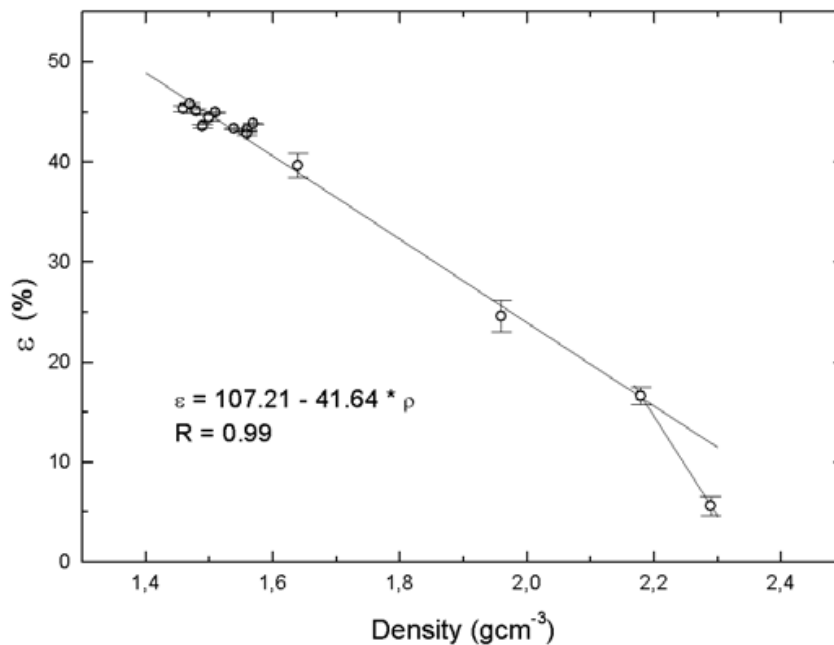


Fig. 8. Correlation between the samples porosity and density. The straight lines correspond to the data linear regression

Sample	Volumetric Shrinkage (%)	Bending Strength (MPa)	Water Absorption (%)
J Clay	2.1	3.3	20.3
J Clay 30	1.5	2.6	20.9

Table 4. Technological properties of end-product ceramic (~980 °C) without residue (J clay) and with 30 wt.% of sanitary ware residue (J Clay 30)

Comparing the Kaolinitic CG clay and the illitic J clay, we noted that the volumetric shrinkage value of J clay is half of the value of CG clay. In this case, J clay has advantages for the ceramic serial production in relation to dimensions uniformity. On the other side, CG clay presents a double value of bending strength, in relation to the J clay, i. e., more resistant pieces are shaped.

5. Thermal characterisation of CG and J clays using photothermal techniques, in relation to structural changes on firing

By analysing the thermal properties, some information can be collected from the material. In the following, we define the thermal properties and point out the values and their correlations with the sample microstructure.

Thermal diffusivity, a particular property that evaluates the heat propagation behaviour within the sample, is quite sensitive to the material structure as well as preparation and sintering conditions.

When values of thermal diffusivity (α) are evaluated from the amplitude data of the photoacoustic signal, we should pay attention to the microphone non-linear frequency response in relation to acoustic vibrations. Practically, all microphones present this irregularity. In our case, our microphone had a good linear frequency response above 20 Hz. In order to certify our set-up, a calibration measurement was performed. Figure 9 shows the dependence of the photoacoustical (PA) signal on the modulation frequency for the aluminium (Al) sample.

For frequencies used in this work, the signal exhibited a frequency dependency close to $f^{-1.5}$. This is the typical behaviour we would expect from the thermal diffusion model for a thermally thin sample. In fact, for a 25 μm thick Al sample and a thermal diffusivity of $93.28 \times 10^{-6} \text{ m}^2/\text{s}$ (Almond and Patel, 1996) the characteristic frequency f_c for the transition between the thermally thin and thick regime is about 47.5 kHz.

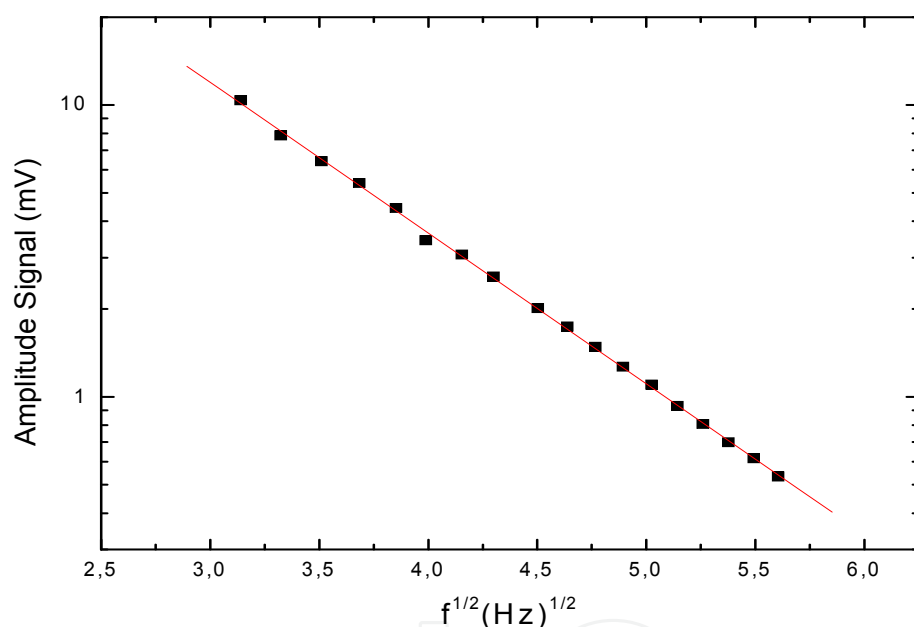


Fig. 9. Microphone output voltage as a function of the chopping frequency for the 25 μm thick Al sample. The signal behaves roughly as $f^{-1.5}$

The thermal conductivity (κ) is associated with thermal conduction, which is the phenomenon where the heat is carried from regions of high temperature to regions of low temperature in a material.

The thermal effusivity (ϵ) denotes the material thermal impedance and is a measurement of the heat energy stored in a solid per degree of temperature rise from the start of a surface heating process (Marín *et al.*, 2002).

Here, thermal conductivity and thermal effusivity are reached applying the following expressions:

$$k = \alpha \rho c \tag{2}$$

$$\varepsilon = \sqrt{k\rho c} \quad (3)$$

Experiments concerning with thermal diffusivity, samples thickness and specific heat capacity measurements were performed five, ten and three times to produce the deviations, respectively.

5.1 Thermal diffusivity measurement

The thermal diffusivity experimental set-up is shown in Fig. 10. The sample is mounted directly onto a commercial electret microphone (Omnidirectional back electret condenser microphone cartridge, model WM-61A - Panasonic), fixed with a silicone grease, illuminated by the light beam from a He-Ne laser (Unilaser mod. 025) and modulated with a mechanical chopper (EG&G Instruments mod. 651), before it reaches the sample's surface. It consists of an OPC configuration in the sense that the sample is placed on top of the detection set-up itself (Vargas and Miranda, 1988). As a result of the periodic sample heating by modulated light absorption, the pressure inside the cell oscillates at the chopping frequency and can be detected by the microphone. The resulting PA signal is then subsequently fed into a field-effect-transistor (FET) pre-amplifier and leads directly to a "Lock-in" amplifier (Perkin Elmer Instruments mod. 5210), where it is possible to obtain the photoacoustic amplitude and the phase signal, which are recorded as a function of the modulation frequency in an appropriate software program.

According to the model proposed by (Rosencwaig and Gersho, 1976) for thermal diffusion, the equation that leads us to the pressure fluctuation (δP) in the air chamber is

$$\delta P = \frac{\gamma P_0 I_0 (\alpha_g \alpha_s)^{1/2} \exp j(\omega t - \pi/2)}{2\pi l_g T_0 k_s f \sinh(\sigma_s l_s)}, \quad (4)$$

where γ is the air specific heat ratio, P_0 the ambient pressure, T_0 ambient temperature, I_0 is the absorbed light intensity, f is the modulation frequency, and l_i , k_i and α_i are the length, thermal conductivity and the thermal diffusivity of the sample, respectively. Here, the subscripts denote the absorbing samples (s) and the gas (g) media, respectively, and $\sigma_i = (1 + j)\alpha_i$, is the complex thermal diffusion coefficient of i medium. It is assumed in the Eq. 4 that the sample is optically opaque $l_\beta \ll l_s$, where l_β is the optical penetration depth. For thermally thin sample $\mu_s > l_s$; $f < f_c$, where μ_s is the thermal diffusion length and $f_c = \alpha/\pi l_s^2$ is the cut-off frequency, Eq. 4 reduces to

$$\delta P = \frac{\gamma P_0 I_0 (\alpha_g)^{1/2} \alpha_s \exp j(\omega t - 3\pi/4)}{2\pi^{3/2} T_0 l_g l_s k_s f^{3/2}} \quad (5)$$

Here, the amplitude of the PA signal decreases as $f^{-1.5}$. On the other hand, at modulation frequencies above f_c , the sample is regarded as thermally thick and the corresponding equation is

$$\delta P = \frac{\gamma P_0 I_0 (\alpha_g \alpha_s)^{1/2} \exp -l_s \sqrt{\pi f / \alpha_s} \exp j(\omega t - \pi/2 - l_s \alpha_s)}{\pi l_g T_0 k_s f} \quad (6)$$

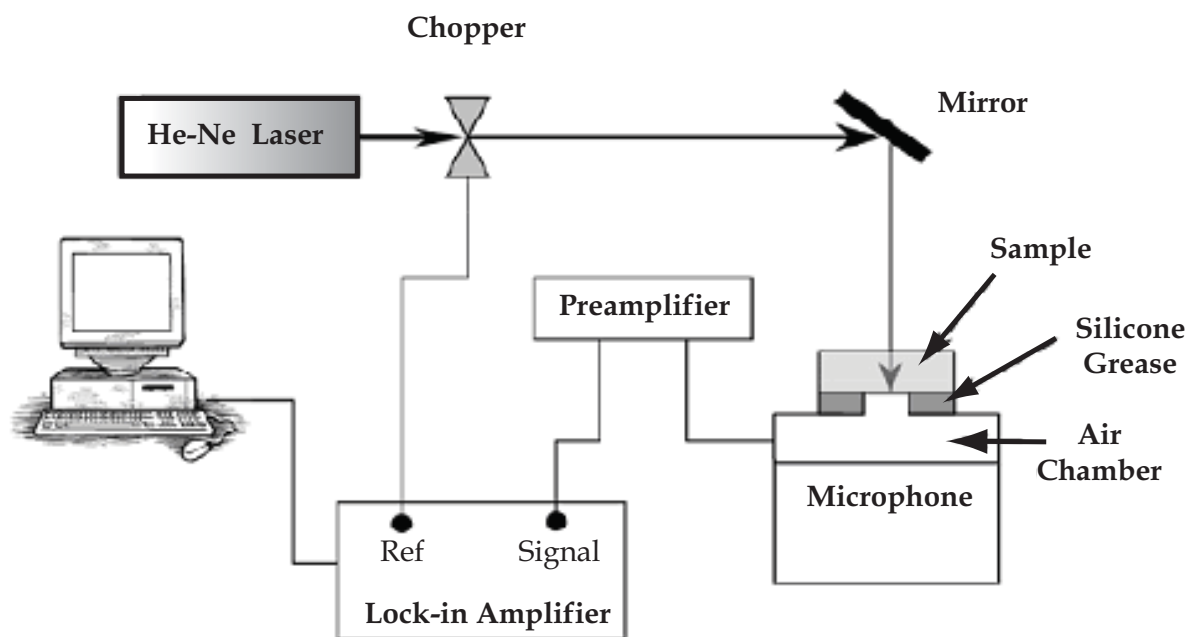


Fig. 10. Experimental arrangement for the thermal diffusivity measurements following (Yunus *et al.*, 2002)

The amplitude of the PA signal for a thermally thick sample decreases exponentially with the modulation frequency as $S_{PA} \propto 1/f \exp(-b\sqrt{f})$, where $b = l_s \sqrt{\pi/\alpha_s}$. In this case, α_s is obtained from the experimental data fitting from the parameter b .

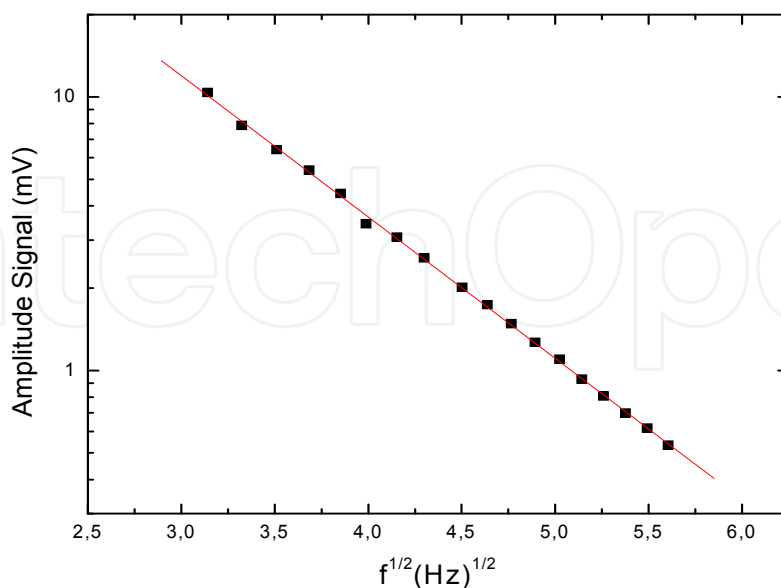


Fig. 11. Photoacoustic signal amplitude measurements as a function of the frequency square root for the 900 °C sample, together with the theoretical line

Taking values of thermal diffusivity from the literature, the cut-off frequency f_c is about 5.87 Hz, i.e. the frequency domain is regarded as thermally thick. As an example, Fig. 11 shows one of our sets of experimental points and the theoretical line for the 900 °C sample.

5.2 Specific heat capacity measurement

Specific heat capacity illustrates how a material can store large amount of heat, without suffering drastic temperature changes. The specific heat capacity (ρc) was measured using the photothermal technique of temperature evolution induced by continuous illumination of the sample in vacuum. The sample surface was painted black to make the parameter characterising the radiative properties of the surface equals to unit ($\epsilon = 1$) and placed inside a Dewar, which is subsequently vacuum-sealed, As shown in Fig. 12. The front surface was illuminated by the He-Ne laser focused on the sample through an optical glass window on the Dewar. On the sample backside was connected a thin-wire T-type thermocouple. The thermocouple output was measured as a function of time by using a thermocouple monitor (Model SR630, Stanford Research Systems) attached to a computer. Care has been taken to prevent the heating light from reaching the thermocouple. Since the sample thicknesses, typically of the order of micrometers was much smaller than their widths (e.g., 10 mm), the simple one-dimensional heat diffusion equation with radiation losses can be applied to our experiment (Mansanares *et al.*, 1990).

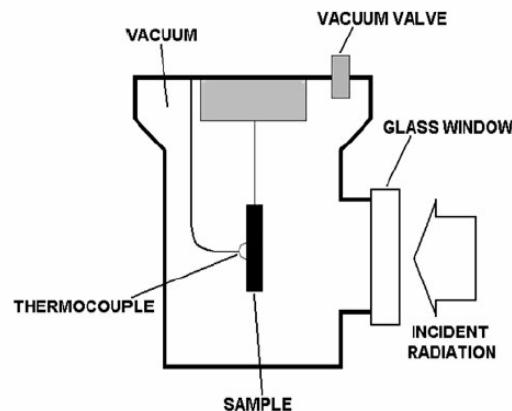


Fig. 12. Experimental arrangement for the specific heat capacity measurements

The temperature evolution was monitored from the ambient temperature up to the sample temperature saturation, obeying Eq. 7 and then the light was turned off and the temperature variation recorded until it reached the ambient temperature again (Eq. 8).

$$\Delta T \uparrow = \frac{I_0}{H} (1 - \exp(-t / \tau)) \quad (7)$$

$$\Delta T \downarrow = \frac{I_0}{H} \exp(-t / \tau) \quad (8)$$

Here, I_0 is the incident light intensity, $\tau = l\rho c / 2H$ is the thermal relaxation time, $H = 4\sigma T_0^3$ is the heat transfer coefficient, where σ is the Stefan-Boltzmann constant, T_0 is the ambient temperature and t is the time variable (Mota *et al.*, 2008).

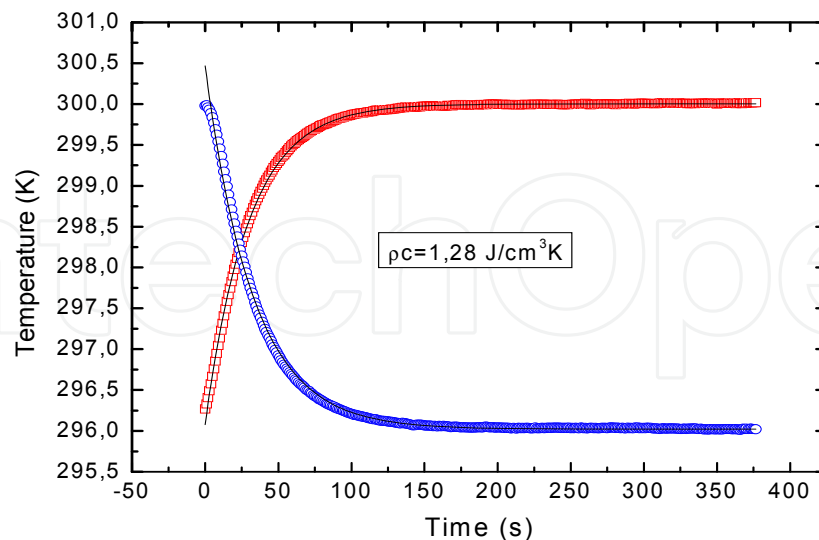


Fig. 13. Experimental data and theoretical lines of rising (square) and decreasing (circle) temperatures as a function of time for the 1060 °C sample

As an example, Fig. 13 shows the experimental data (open symbols) and theoretical lines for the 1060 °C sample (CG clay).

5.3 Results and discussion

Results of measurements of the thermal properties from CG clay are shown in Table 5 as a function of firing temperature.

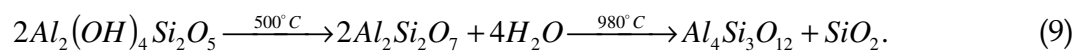
Temperature (°C)	Thickness (µm)	Thermal diffusivity (cm ² /s)	Specific heat capacity (J/cm ³ K)	Thermal conductivity (W/cmK)	Thermal effusivity (Ws ^{1/2} /cm ² K)
900	275±1.56%	0.012±2.58%	1.367±4.13%	0.016	0.148
950	273±3.58%	0.025±4.96%	1.064±3.08%	0.027	0.168
980	419±0.61%	0.012±2.99%	1.178±3.64%	0.014	0.129
1020	323±1.41%	0.021±2.16%	1.201±1.34%	0.025	0.174
1060	330±0.63%	0.031±0.22%	1.141±2.14%	0.035	0.200
1100	323±1.56%	0.013±2.58%	1.067±1.37%	0.014	0.122

Table 5. Thermal properties values and samples thickness as a function of firing temperature with its standard deviation

Thermal diffusivity values ranged from 0.0016 to 0.0063 cm²/s and are in close agreement with the literature (Alexandre *et al.*, 1999; García *et al.*, 2002). Table 5 presents values for specific heat capacity that were around 1.0 (J/cm³K). Thus, we can infer that thermal conductivity and effusivity tend to follow the thermal diffusivity profile in relation to the firing temperature. Moreover, for this kind of material, thermal properties are strongly dependent on the material microstructure.

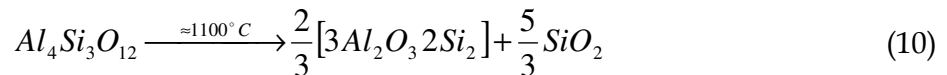
In relation to the structure, Fig. 1 shows the evolution of the X-ray diffraction patterns as a function of firing temperature. For natural clay the diffractogram reveals predominant phases of kaolinite, quartz and small amounts of gibbsite, illite, orthoclase and anatase. Following the treatment at 900 °C, illite, quartz, anatase and orthoclase remain unchanged and a hematite phase is revealed. Treatments at 950 °C or higher cause sample recrystallization in the Al-Si spinel (Okada *et al.*, 1986) and a liquid phase formation. Data clearly show the evolution of mullite and cristobalite in samples over the temperatures 1060 °C and 1100 °C.

Analysing the thermal diffusivity and the diffractograms, we can explain that the lower diffusivity value in 980 °C and 1020 °C is possibly due to the Al-Si rearrangements, owing to a crystallization process followed by a lattice formation (Okada *et al.*, 1986), according to



Equation 9 shows kaolinite $2Al_2(OH)_4Si_2O_5$ evolution, which reaches the spinel phase $Al_4Si_3O_{12} + SiO_2$ formation, with an intermediate phase, namely metakaolin $2Al_2Si_2O_7 + 4H_2O$. The high diffusivity value at 1060 °C could possibly be connected to the liquid phase formation within the beginning of the vitreous phase. The heat can be transported easier in this kind of phases than through the clay mineral grains. In support of this explanation for the highest thermal diffusivity, we note the clear modification of structure shown to occur above 1060 °C.

At 1100 °C, the thermal diffusivity decreases as explained by the reaction.



Through sintering at this temperature, formation of mullite $\frac{2}{3}[3Al_2O_3 \cdot 2Si_2]$ and cristobalite $\frac{5}{3}SiO_2$ starts from the spinel phase $Al_4Si_3O_{12}$, as reported by references in (Okada *et al.*, 1986). We suggest that there is a reduction of liquid phase and pores, with the formation of cristobalite, which probably is responsible for the thermal diffusivity decay.

Summarizing, the red clay from Campos dos Goytacazes-RJ region are used mainly for bricks and roofing tiles. In general, ceramic plants fire their products at temperatures below 900 °C. In the raw state the red clay, as shown in Fig. 1, is composed of a high proportion of kaolinite clay mineral besides accessory minerals including oxy-hydroxide, illite, quartz, and anatase. In this case sintering is dominated by particle-to-particle contact mainly of metakaolinite platelets, resulting in a more open structure and also ceramic products of low quality. High porosity results in a lower thermal diffusivity and thermal conductivity. On the other hand, the sintering accelerates above 950 °C with drastic microstructural changes due to the formation of a vitreous phase, resulting in better densification behaviour of the red clay. As a consequence, the thermal diffusivity increases abruptly. However, a decrease in the thermal diffusivity occurred between 1060 °C - 1100 °C. This is due mainly to formation of mullite, which is characterized by a high proportion of oxygen vacancies that lead to low thermal diffusivity. It will be reasonable then to consider that the optimum firing temperature range for the studied red clay is above 950 °C.

Temperature (°C)	Thermal diffusivity (cm ² /s)	Specific heat capacity (J/cm ³ K)	Thermal conductivity (W/cm K)	Thermal effusivity (Ws ^{1/2} /cm ² k)
900	0.003 ± 0.0004	0.61 ± 0.11	0.002 ± 0.00	0.034 ± 0.0013
950	0.005 ± 0.0000	0.83 ± 0.02	0.004 ± 0.00	0.061 ± 0.0005
1000	0.007 ± 0.0000	0.82 ± 0.13	0.006 ± 0.00	0.072 ± 0.0008
1050	0.004 ± 0.0000	0.92 ± 0.09	0.004 ± 0.00	0.061 ± 0.0001
1100	0.004 ± 0.0002	0.67 ± 0.11	0.003 ± 0.01	0.045 ± 0.0010

Table 6. Thermal properties of the J clay as in function of some possible sintering temperatures

Temperature (°C)	Thermal diffusivity (cm ² /s)	Specific heat capacity (J/cm ³ K)	Thermal conductivity (W/cm K)	Thermal effusivity (Ws ^{1/2} /cm ² k)
900	0.008 ± 0.0001	0.98 ± 0.00	0.007 ± 0.00	0.088 ± 0.0011
950	0.004 ± 0.0005	1.12 ± 0.15	0.005 ± 0.11	0.072 ± 0.0008
1000	0.009 ± 0.0008	1.57 ± 0.04	0.014 ± 0.08	0.148 ± 0.0005
1050	0.006 ± 0.0004	1.43 ± 0.17	0.008 ± 0.06	0.111 ± 0.0010
1100	0.004 ± 0.0009	1.25 ± 0.02	0.005 ± 0.09	0.082 ± 0.0009

Table 7. Thermal properties of the J clay with 30% sanitary ware mass residues as in function of some possible sintering temperatures

Tables 6 and 7 show the thermal properties of the J clay and J clay with 30% residue, respectively.

Regarding to the ceramic thermal properties, the CG clay ceramic sample presented much higher values than the J clay ceramic. Thus, depending on the application, considering thermal properties we can use a kaolinite raw material if we need ceramics with fast thermalization or illitic clays for a better thermal isolation. We noted that the aggregation of 30% of sanitary ware mass residue in the J clay matrix generates higher values of the ceramic thermal properties.

6. Pollutant gases from the firing of clay ceramic added with residues

The gas emission concentrations during the CG and J clays firing process were measured. The figures were displayed in such way that it is possible to compare the whole samples for each gas, obeying the CG clay samples and the J clay samples.

6.1 Experimental procedure

The following materials were studied in this present research: **a)** the CG clay and steel slag considered as a waste by the National Steel Plant (CSN) located at the south of the state. This slag was generated during the conventional oxygen blowing, LD (Linz Donawitz) process, of steel refining; **b)** The J clay and the sanitary ware mass rejects from a ceramic industry of São Paulo state.

The emitted gases from the firing process were quantitatively measured by means of a photothermal technique.

The gas released from the furnace was directly connected to an infrared model URAS 14, ABB gas analyser under a suction flux of 0.3 L/min. This gas analyser detected and quantified simultaneously CO, CO₂, CH₄, NO, N₂O, NH₃ e SO₂. Gas samples were collected 20 min. after settled temperature stages of respectively, 150, 300, 450, 550, 650, 800, 950, 1050 and 1100 °C. The samples were brought to room temperature following the inertial cooling of the resistive furnace.

The gas analyser measurement process is based on resonance absorption at the characteristic vibrational rotation spectrum bands of non-elemental gases in the middle infrared range between 2 µm and 12 µm. Because of their bipolar moment, the gas molecules interact with infrared emissions. For selectivity, the receiver is filled with the applicable sample components to establish reference and sensitivity to these components (~1 ppm). It consists of the cell divided into two identical compartments: one in the measuring cell, through which the sampled gas is flowed, and the other acts as reference, filled with nitrogen. The light emitted from a hot filament is modulated by a mechanical chopper and divided by a beam splitter. Each beam goes simultaneously through the measuring cell and the reference cell. The detector consists of two sealed chambers separated by a diaphragm capacitor. Both chambers are filled with pure gas of the chemical species under study. The light beams emerged from the sample and reference cells reach independently the two detector chambers, causing a differential pressure that is proportional to the light absorption by the sample. The pressure difference is converted by the diaphragm capacitor into an electrical signal. A detailed description of the Uras performance can be found in the literature ⁽¹¹⁾. Before each sample analyses the cells were calibrated using pure standard N₂.

6.2 Results and discussion

Figures 14 and 15 show the released CO₂ and CO gases as in function of the temperature from the CG clay with (5%, 10%) and without (0%) steel slag residue in different concentrations in weight. The other gases had not presented significant values.

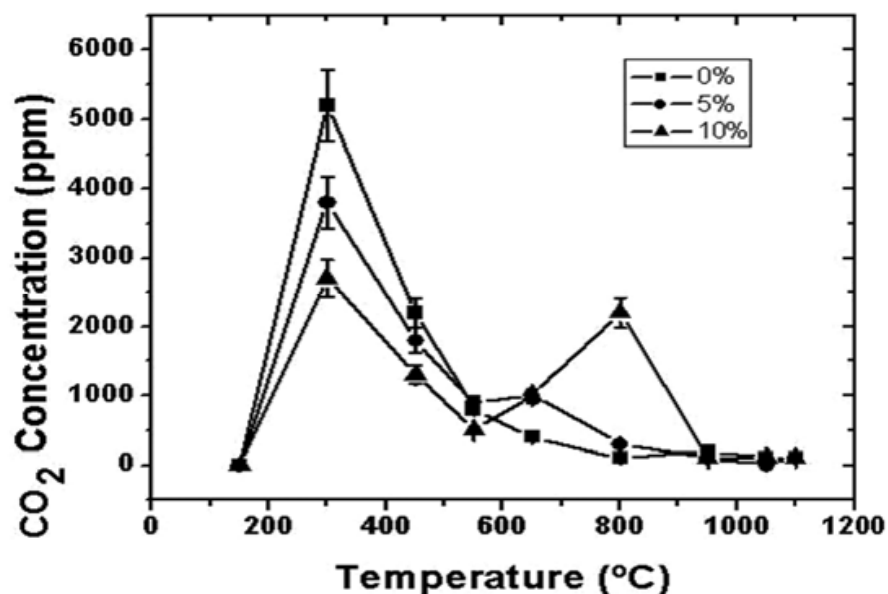


Fig. 14. CO₂ profiles as in function of the firing temperature for the samples with 0 %, 5 %, and 10 %

CO₂ concentration values were emitted more significantly in the presence of the residue. Generally, carbon composites, as CO₂, in the range of 300 °C to 500 °C are emitted due to the organic matter oxidation. Moreover, the reaction of the kaolinite and goethite dehydroxilation deals to a metakaolinite, that is, an amorphous phase.

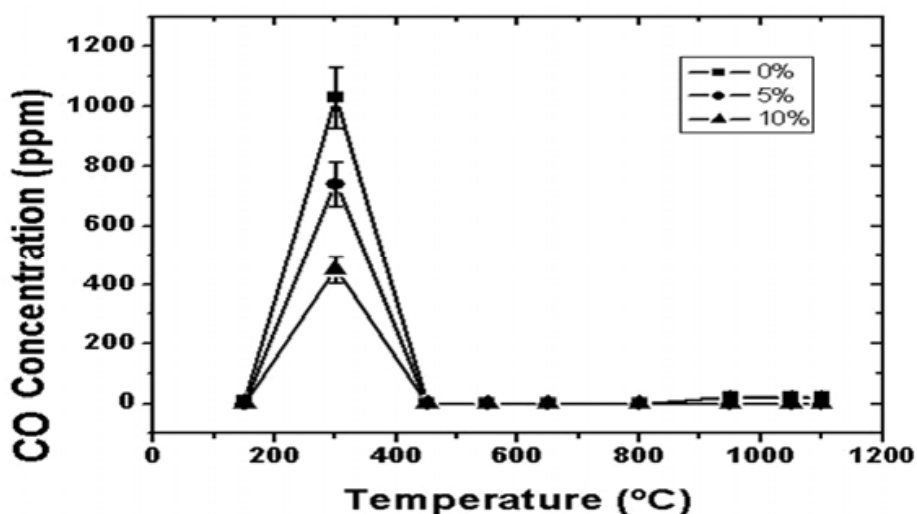


Fig. 15. CO profiles as in function of the firing temperature for the samples with 0 %, 5 %, and 10 %

The CO₂ emission in temperatures higher than 850 °C, is possibly due to: the hydroxil (OH) release, proceeding from the gases that were locked up in the pores, which are set free later when the pores begin processes of volumetric reduction, due to the high temperature; the chemical dehydration of minerals that contains mica (muscovite); and the calcite decomposition ($\text{CaCO}_3 = \text{CaO} + \text{CO}_2$). Values reached in this section were just proportional to a laboratory furnace.

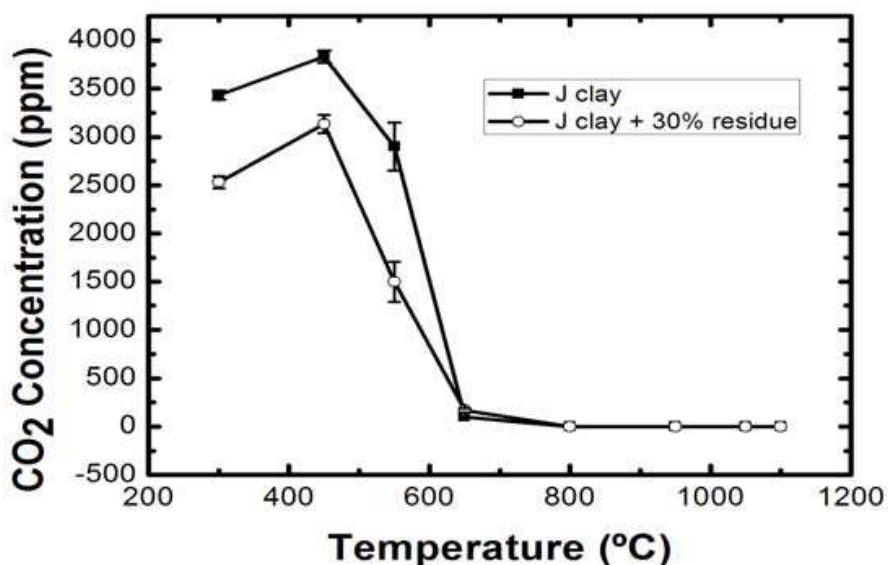


Fig. 16. CO₂ emitted during the ceramic firing process as in function of the firing temperature

Figures 16 and 17 show the CO₂ and CO emissions as in function of firing temperature from the J clay without and with 30% in weight of sanitary ware mass residue. Firstly, we observed that the addition of the residue diminishes the amount of CO₂ emission. The amount of CO₂ emitted between 300 and 550 °C has the same explanation previously cited, that is, due to organic matter oxidation and the dehydroxilation of clay minerals.

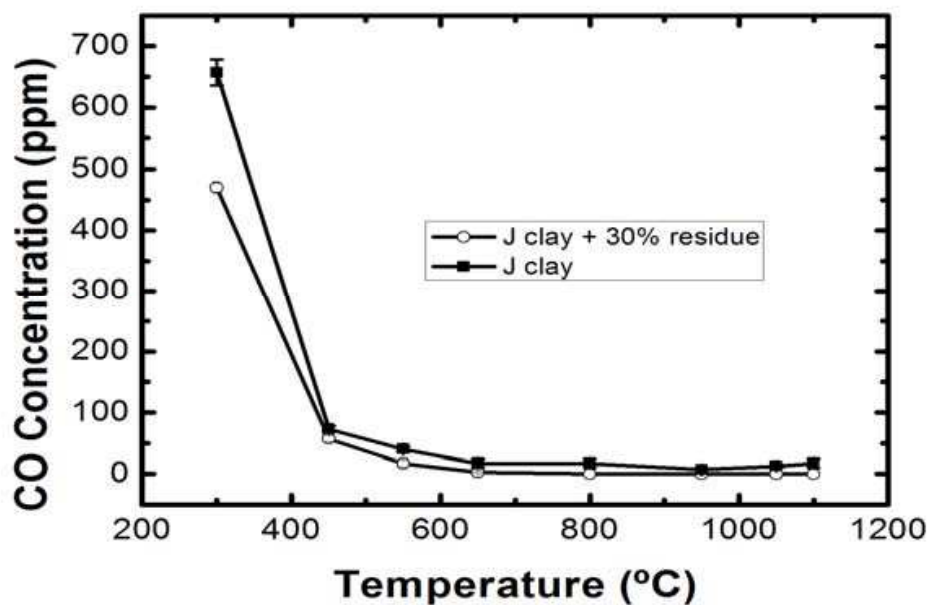


Fig. 17. CO emitted during the ceramic firing process as in function of the firing temperature

7. Conclusions

Here, red ceramic samples from Rio de Janeiro state and from São Paulo state were analysed as in function of firing temperature. In order to study the ceramics quality, technological essays were prepared. Comparisons between the Kaolinite CG clay and the illitic J clay were made, indicating the advantages and disadvantages of each specimen.

The thermal property of red ceramic samples as well as their crystalline phases were analysed as a function of sintering temperature. Photothermal techniques were used to measure the thermal properties and the microstructures were identified by x-ray diffraction, in order to compare structural and thermal features of the samples. It was shown that there is an intrinsic relationship between the structure and the thermal diffusivity. When the crystalline structure undergoes strong perturbations the thermal diffusivity values decrease and vice-versa. When liquid phases achieve the highest concentration at around 1060 °C (CG clay) and 1000 °C (J clay), the thermal diffusivity shows its maximum peak. Afterwards, there is a decrease, although the thermal diffusivity maintains high values, due to mullite enhancement and vitreous phase consolidation in the red ceramics. The J clay sintering temperature is lower than to the CG clay, due to a larger amount of flux material.

Thermal property values are consistent with the literature. As the specific heat capacity has values of approximately unity, thermal conductivity and effusivity follow that of thermal diffusivity. Considering thermal properties, it was shown that red ceramic sintering temperatures should be greater than 950 °C, but below 1060 °C from both clays.

The steel slag investigated, considered as a steelmaking waste, has an elevated amount of Ca, Fe, Mg and Si. The main crystalline phases identified were magnetite, Fe_3O_4 , calcite, CaCO_3 , magnesium manganese oxide, Mg_6MnO_8 and calcium silicate, Ca_2SiO_4 , CaSiO_3 . The incorporation of steel slag into clayey ceramics, must be done in amounts of up to 10 wt.%. In relation to the steel slag incorporation, it had been mainly detected CO and CO_2 . Comparing the diverse percentages of residues into the ceramic mass, it observed that the CO_2 concentrations decrease in the range of 300 °C to 500 °C, when increased the percentage of residue to the mass. On the other side, between 500 °C and 950 °C, there was a reasonable increase of the concentration (in relation to the pure clay), when the residues percentage was enlarged. The calcite starts to decompose around 675 °C and its complete decomposition occurs up to 950 °C. When mixed to another minerals, the calcite presents lower temperature of decomposition (880 °C, approximately).

It is possible that sanitary ware residues can attenuate the pollutant gas release from the ceramic firing. We concentrate in this chapter the CO and CO_2 gases, in order to facilitate the point of view of our study. It will appear elsewhere the complete set of measured gases from this research.

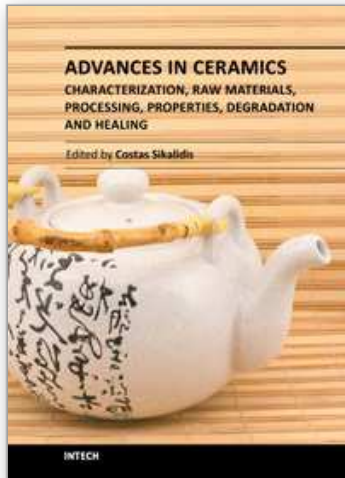
8. Acknowledgment

The authors thank the Brazilian agencies FAPERJ, CNPq and CAPES for the financial support.

9. References

- Alexandre, J.; Saboya, F.; Marques, B. C.; Ribeiro, M. L. P.; Salles, C., da Silva, M. G.; Sthel, M. S., Auler, L. T. & Vargas, H. (1999). Photoacoustic thermal characterization of kaolinite clays. *The Analyst*, vol. 124, pp. 1209 -1214.
- Almond, D.P., & Patel, P.M. (1996). *Photothermal Science and Techniques*. Chapman & Hall, London.
- Dubois, J.; Murat, M.; Amroune, A.; Carbonneau, X. & Gardon, R. (1995). High-temperature transformation in kaolinite: the role of the crystallinity and of the firing atmosphere. *Appl. Clay Science*, vol. 10, pp. 187-198.
- Faria Jr., R.T.; Filgueira, M.; Esquef, I.A.; Machado, F.A.; Rodrigues, M.F.; Bobrovnichii, G.S. & Vargas, H. (2005). Thermal characterization of sintered hardmetal. *Journal de Physique. IV*, vol. 125, pp. 237-239.
- García, E., Osendi, M.I., Miranzo, P., 2002. Thermal diffusivity of porous cordierite ceramic burners. *Journal of Applied Physics* 92, 2346-2349.
- Heydorn, K. & Thuesen, I. (1989). Classification of ancient Mesopotamian ceramics and clay using SIMCA for supervised pattern recognition. *Chemometrics and Intelligent Laboratory Systems*, vol.7, pp. 181-188.
- Manhães, R. S. T.; Auler, L. T.; Sthel, M. S.; Alexandre, J.; Massunaga, M. S. O.; Carrió, J. G.; dos Santos, D. R.; da Silva, E. C.; Garcia-Quiroz, A. & Vargas, H. (2002). Soil characterisation using X-ray diffraction, photoacoustic spectroscopy and electron paramagnetic resonance. *Appl. Clay Science*, vol. 21, pp. 303.
- Mansanares, A.M.; Bento, A.C.; Vargas, H., Leite, N.F. & Miranda, L.C.M. (1990). Photoacoustic measurement of the thermal properties of two-layer systems. *Physical Review B*, vol. 42, pp. 4477-4486.

- Marín, E.; Marín-Antuna, J. & Díaz-Arencibia, P. (2002). On the wave treatment of the conduction of heat in photothermal experiments with solids. *European Journal of Physics*, vol. 23, pp. 523-532.
- Morgan, D. J. (1993). Thermal analysis including evolved gas analysis of clay raw materials, *Applied Clay Science*, vol. 8, pp. 81.
- Mota, L.; Toledo, R. ; Machado, F.A.L.; Holanda, J.N.F.; Vargas, H. & Faria Jr., R.T. (2008). Thermal characterization of red clay from the Northern Region of Rio de Janeiro State, Brazil using an open photoacoustic cell, in relation to structural changes on firing. *Appl. Clay Science*, vol. 42, pp. 168-174.
- Nastro, V.; Vuono, D.; Guzzo, M.; Niceforo, G.; Bruno, I. & de Luca, P. (2006). Characterisation of raw materials for production of ceramics. *Journal of Thermal Analysis Calorimetry*, vol. 84, pp. 181-184.
- Okada, K.; Otsuka, N. & Ossaka, J. (1986). Characterization of spinel phase formed in the kaolin-mullite thermal sequence. *J. Am. Ceram. Soc.*, vol. 69, pp. C251-C253.
- Oliveira, G.E., & Holanda, J.N.F., (2004). Utilization of solid waste from siderurgical industry in red ceramic, *Cerâmica*, vol. 50, pp. 75-80.
- Parsons, A. J.; Inglethorpe, S. D. J.; Morgan, D. J. & Dunham, A. C. (1997). Evolved gas analysis (EGA) of bricks clays. *J. Therm. Analysis*, vol. 48, pp.49.
- Perondi, L.F. & Miranda, L.C.M. (1987). Minimal volume photoacoustic cell measurement of thermal diffusivity: effect of the thermoelastic sample bending. *Journal of Applied Physics* , vol. 62, pp. 2955-2959.
- Reed J.S. (1976). *Principles of the Ceramics Processing*. John Wiley and Sons, New York.
- Rice, R.W. & Dekker, M. (1998). *Porosity of Ceramics*, Elsevier, New York
- Rosencwaig, A. & Gersho, A. (1976). Theory of the photoacoustic effect with solids. *Journal of Applied Physics*, vol. 47, pp. 64-69
- Souza, V.P.; Toledo, R.; Holanda, J.N.F.; Vargas, H. & Faria Jr, R.T. (2008). Pollutant gas analysis evolved during firing of red ceramic incorporated with water treatment plant sludge. *Cerâmica*, vol. 54, pp. 351-355.
- Vargas, H. & Miranda, L.C.M. (1988). Photoacoustic and related photothermal techniques. *Physics Reports*, vol. 161, pp. 43-101.
- Vieira, C.M.F. & Monteiro, S.N. (2009). Incorporation of solid wastes in red ceramics: an updated review. *Matéria (Rio J.)*, vol.14, nº .3, pp. 881-905. ISSN 1517-7076.
- Yunus, W.M.M.; Fanny, C.Y.J.; Phing, T.E.; Mohamed, S.B.; Halim, S.A. & Moskin, M.M. (2002). Thermal diffusivity measurement of Zn, Ba, V, Yand Sn doped Bi-Pb-Sr-Ca-Cu-O ceramics superconductors by photoacoustic technique. *Journal of Material Science*, vol. 37, pp. 1055-1060.



Advances in Ceramics - Characterization, Raw Materials, Processing, Properties, Degradation and Healing

Edited by Prof. Costas Sikalidis

ISBN 978-953-307-504-4

Hard cover, 370 pages

Publisher InTech

Published online 01, August, 2011

Published in print edition August, 2011

The current book consists of eighteen chapters divided into three sections. Section I includes nine topics in characterization techniques and evaluation of advanced ceramics dealing with newly developed photothermal, ultrasonic and ion sputtering techniques, the neutron irradiation and the properties of ceramics, the existence of a polytypic multi-structured boron carbide, the oxygen isotope exchange between gases and nanoscale oxides and the evaluation of perovskite structures ceramics for sensors and ultrasonic applications. Section II includes six topics in raw materials, processes and mechanical and other properties of conventional and advanced ceramic materials, dealing with the evaluation of local raw materials and various types and forms of wastes for ceramics production, the effect of production parameters on ceramic properties, the evaluation of dental ceramics through application parameters and the reinforcement of ceramics by fibers. Section III, includes three topics in degradation, aging and healing of ceramic materials, dealing with the effect of granite waste addition on artificial and natural degradation bricks, the effect of aging, micro-voids, and self-healing on mechanical properties of glass ceramics and the crack-healing ability of structural ceramics.

How to reference

In order to correctly reference this scholarly work, feel free to copy and paste the following:

Faria Jr. R. T., Souza V. P., Vieira C. M. F., Toledo R., Monteiro S. N., Holanda J. N. F. and Vargas H. (2011). Characterization of Clay Ceramics Based on the Recycling of Industrial Residues – On the Use of Photothermal Techniques to Determine Ceramic Thermal Properties and Gas Emissions during the Clay Firing Process, *Advances in Ceramics - Characterization, Raw Materials, Processing, Properties, Degradation and Healing*, Prof. Costas Sikalidis (Ed.), ISBN: 978-953-307-504-4, InTech, Available from: <http://www.intechopen.com/books/advances-in-ceramics-characterization-raw-materials-processing-properties-degradation-and-healing/characterization-of-clay-ceramics-based-on-the-recycling-of-industrial-residues-on-the-use-of-photot>



InTech Europe

University Campus STeP Ri
Slavka Krautzeka 83/A
51000 Rijeka, Croatia
Phone: +385 (51) 770 447

InTech China

Unit 405, Office Block, Hotel Equatorial Shanghai
No.65, Yan An Road (West), Shanghai, 200040, China
中国上海市延安西路65号上海国际贵都大饭店办公楼405单元
Phone: +86-21-62489820

Fax: +385 (51) 686 166
www.intechopen.com

Fax: +86-21-62489821

IntechOpen

IntechOpen

© 2011 The Author(s). Licensee IntechOpen. This chapter is distributed under the terms of the [Creative Commons Attribution-NonCommercial-ShareAlike-3.0 License](#), which permits use, distribution and reproduction for non-commercial purposes, provided the original is properly cited and derivative works building on this content are distributed under the same license.

IntechOpen

IntechOpen